PHYSICAL REVIEW B **82**, 180503(R) (2010)

Nonlocal conductance via overlapping Andreev bound states in ferromagnet-superconductor heterostructures

Georgo Metalidis,[1] Matthias Eschrig,[1,2] Roland Grein,[1] and Gerd Schön[1]
[1]*Institut für Theoretische Festkörperphysik and DFG-Center for Functional Nanostructures, Karlsruhe Institute of Technology (KIT), D-76128 Karlsruhe, Germany*
[2]*Fachbereich Physik, Universität Konstanz, D-78457 Konstanz, Germany*
(Received 11 October 2010; published 2 November 2010)

In a setup where two ferromagnetic electrodes are attached to a superconductor, Andreev bound states are induced at both ferromagnet/superconductor (FM/SC) interfaces. We study how these states propagate through the SC and interact with each other. As a result of this interaction, the energetic positions of the Andreev states are not anymore determined solely by the magnetic properties of a single interface but also depend on the interface distance and the relative magnetization orientation of the FM contacts. We discuss how these bound states show up as distinct peaks in the nonlocal conductance signal and lead to marked asymmetries with respect to the applied voltage. We relate our results to nonlocal crossed Andreev and elastic cotunneling processes.

DOI: 10.1103/PhysRevB.82.180503 PACS number(s): 74.45.+c, 73.23.−b, 74.78.Na

Surface states in solid-state physics have inspired a renewed strong activity, as they lead to insight into fundamental questions related to topology, conflicting types of order, or new types of excitations. Examples are spin Hall effect edge states in mercury-telluride quantum wells and other topological insulators[1] or Andreev surface states in unconventional superconductors.[2] The presence of Andreev bound states (ABS) at energies below the superconducting gap plays a prominent role in transport through heterostructures involving superconductors and forms a topic of continuing and long-standing interest. Such states can arise, e.g., due to multiple Andreev reflections at both interfaces of a SC-insulator-SC junction and are directly related to the Josephson current through the junction.[2] Furthermore, the importance of a magnetically active interface between a SC and FM has been pointed out. Scattering on such a surface leads to spin mixing and the creation of subgap ABS at the SC/FM interface.[3,4] Such states influence the properties of, e.g., single SC/FM tunnel junctions[5,6] and SC/FM/SC Josephson junctions.[4,7,8]

When two metallic leads are connected to a SC, an electron injected into the SC from one lead can combine to form a Cooper pair with an electron from the other lead, leaving a hole.[9] This so-called crossed Andreev reflection (CAR) process competes with elastic cotunneling (EC), in which the incident electron is transmitted to the other lead via virtual states in the SC. Thus, the nonlocal (NL) conductance,[10] i.e., the current response in one lead to the voltage bias in the other has opposite sign for CAR and EC. In fact, CAR and EC processes cancel each other for tunnel contacts.[11] This cancellation is lifted at higher orders in the transmission,[12] for FM contacts,[11–14] or in the presence of interactions.[15] Disorder effects have also been addressed.[16] Although solid theoretical progress has been made, the role of ABS in the NL conductance has not been elucidated.

In this Rapid Communication, we consider the nonlocal setup shown in Fig. 1, where two FM point contacts are attached to a ballistic SC region. At each of the two SC/FM contacts subgap ABS form, which show up in the Andreev spectrum.[4,6] They propagate on a coherence length scale ξ through the SC. Interestingly, we find that these states interact with each other so that their energetic position depends on the relative magnetization orientation of the interfaces. We study the profound influence of this interaction on the NL conductance $G_{\mathrm{NL}}=\partial I_{\mathrm{R}}/\partial V_{\mathrm{L}}$ through the device when voltages V_{L} and V_{R} are applied across the contacts. For identical contact parameters, we find that for parallel (P) magnetization, G_{NL} is asymmetric in V_{L}, whereas it stays symmetric in the antiparallel (AP) configuration. Such (a)symmetries are explained with an intuitive picture based on the ABS in the system.

Transport properties of heterostructures involving SCs are conveniently described using quasiclassical (QC) Green's functions (GFs), $\hat{g}(\vec{v}_{\mathrm{F}},\vec{R},\varepsilon)$, which depend on the Fermi velocity $\vec{v}_{\mathrm{F}}$, the spatial coordinate $\vec{R}$, and the quasiparticle energy ε. They are obtained from the microscopic GF by integrating out oscillations on the Fermi wavelength scale and obey the Eilenberger equation

$$i\hbar\vec{v}_{\mathrm{F}}\cdot\nabla_{\vec{R}}\hat{g}+[\varepsilon\hat{\tau}_3-\hat{\Delta},\hat{g}]=\hat{0} \tag{1}$$

subject to the normalization condition $\hat{g}^2=-\pi^2$. The "hat" refers to the 2×2 matrix structure of the propagator in particle-hole (Nambu) space and $\hat{\Delta}$ is the SC order parameter. Within our approach, the exchange energy is incorporated by different Fermi velocities $\vec{v}_{\mathrm{F}\sigma}$ and momenta $\vec{p}_{\mathrm{F}\sigma}$ in the spin bands.[8,17] Thus, all elements of the SC propagators,

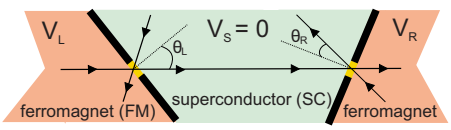

FIG. 1. (Color online) Sketch of the considered FM/SC/FM setup with two tunneling point contacts. A nonlocal scattering event which involves both contacts is indicated.

 ©2010 The American Physical Society

$\hat{g}_{SC}$, are 2×2 spin matrices while the elements of the FM propagators, $\hat{g}_\sigma$, are scalars.

A SC/FM interface enters the QC theory as boundary conditions relating outgoing and incoming propagators.[17] They are expressed in terms of the normal-state scattering matrix S of the interface. We assume that the transmission ($t^{\alpha\beta}$) and reflection coefficients (r^β) of the S matrix are spin diagonal with respect to the magnetization of the FM with diagonal elements $t_\sigma \exp(i\vartheta_\sigma^{\alpha\beta})$ and $r_\sigma \exp(i\vartheta_\sigma^\beta)$, where $\sigma \in \{\uparrow,\downarrow\}$ and $\alpha,\beta \in \{SC,FM\}$.

First we calculate the local density of states (DOS) at points along the line connecting both FM contacts and investigate the ABS interaction. Only the trajectory that connects the two contacts (see Fig. 1) contributes to the subgap DOS at these points; all others emerge from the bulk of the SC and give a zero subgap DOS. Denoting x as the distance from the left electrode, we obtain for this trajectory from the solution of Eq. (1),

$$\frac{N_\sigma(x,\varepsilon)}{N_F} = \frac{1}{2}\mathrm{Re}[(1-\Gamma_{L\sigma}\tilde{\Gamma}_{R\bar{\sigma}})/(1+\Gamma_{L\sigma}\tilde{\Gamma}_{R\bar{\sigma}})], \qquad (2)$$

where N_F is the normal state DOS in the SC and with the notation $\bar{\sigma}=\uparrow(\downarrow)$ when $\sigma=\downarrow(\uparrow)$. The $\Gamma_{i\sigma}$ with $i\in\{L,R\}$ are coherence amplitudes originating from the left (L) and right (R) contact. Their modulus determines the probability for hole-to-particle conversion.[17,18] For subgap energies they are given by[14,17,18]

$$\Gamma_{i\sigma}(x,\varepsilon) = [\Omega\gamma_0 s_{i\sigma} + i(\gamma_0\varepsilon s_{i\sigma}+\Delta)\tanh(\Omega x_i/\Delta\xi)] \times[\Omega - i(\gamma_0\Delta s_{i\sigma}+\varepsilon)\tanh(\Omega x_i/\Delta\xi)]^{-1}. \qquad (3)$$

The $\tilde{\Gamma}_{i\sigma}$ result from $\tilde{\Gamma}_{i\sigma}(x,\varepsilon)=\Gamma^*_{i\sigma}(x,-\varepsilon)$. Here, $\Omega=\sqrt{\Delta^2-\varepsilon^2}$, $\gamma_0=(i\Omega-\varepsilon)/\Delta$, $s_{i\uparrow}=\rho_i e^{i\vartheta_i}$, $s_{i\downarrow}=\rho_i e^{-i\vartheta_i}$, $x_L=x$, $x_R=L-x$ (where L is the distance between the contacts), and $\xi=\hbar v_F^{SC}/\Delta$. Interface properties enter the DOS only via the product $\rho=r_\uparrow r_\downarrow$ and the spin-mixing angle $\vartheta\equiv\vartheta_\uparrow^{SC}-\vartheta_\downarrow^{SC}$ at left and right interface. In the following, we assume for simplicity $\rho=\rho_L=\rho_R$ but allow for differing ϑ_L and ϑ_R. In particular, $\vartheta_R=(-)\vartheta_L\equiv\vartheta$ when speaking of P (AP) magnetization.

In Fig. 2, the DOS is shown at different positions x between the interfaces. ABS appear as distinct spin-resolved subgap peaks. In general, for a positive spin-mixing angle, a spin-up state appears at positive energy. For negative spin-mixing angles, spin-up and spin-down peak positions are interchanged, as expected from Eq. (3). Figure 2 reflects this behavior. For the P case $\vartheta_L=\vartheta_R>0$, the peaks appear at identical energies at the left ($x=0$) and right ($x=L$) interface. For AP magnetization with $\vartheta_L=-\vartheta_R<0$ [Fig. 2(b)] the spin-up (down) state is created at a negative (positive) energy at the left interface, where $\vartheta_L<0$ but at a positive (negative) energy for the right interface, where $\vartheta_R>0$. The DOS peak height decreases on the coherence length scale upon propagation through the SC. For AP magnetization, this leads to two spin-up (and down) states at each interface: the smaller one is created at the opposite interface and is attenuated upon propagation through the SC. This attenuation is less pronounced in the P case, where it is countered by the state coming from the other interface. If $|\vartheta_L|\neq|\vartheta_R|$, ABS

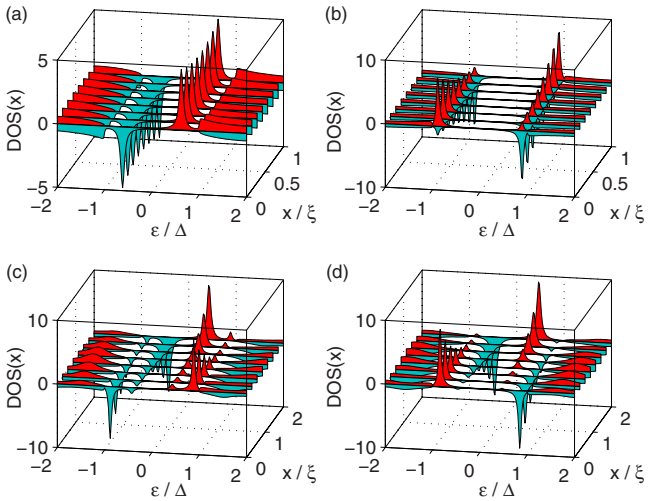

FIG. 2. (Color online) Spin-up (positive axis) and spin-down (negative axis) DOS at different positions x for parallel (left column) and antiparallel magnetization (right column). [(a) and (b)]: $\rho=0.9$, $L=\xi$, and $\vartheta_R=\pm\vartheta_L=0.4\pi$. [(c) and (d)]: $\rho=0.9$, $L=2\xi$,and $\vartheta_L\neq\vartheta_R$ with $\vartheta_L=\pm 0.4\pi$ and $\vartheta_R=0.7\pi$.

have different energies at left and right interface, and their spin-character depends on the spin-mixing angle signs [compare Figs. 2(c) and 2(d)].

These states correspond to poles in Eq. (2). From equating $1+\Gamma_{L\sigma}\tilde{\Gamma}_{R\bar{\sigma}}=0$ and substituting Eq. (3) we obtain in the tunneling limit ($\rho_L=\rho_R=1$),

$$\cos\left(\psi+\frac{\vartheta_L}{2}\right)\cos\left(\psi+\frac{\vartheta_R}{2}\right) = e^{-(2L/\xi)\cos\psi}\sin\left(\frac{\vartheta_L}{2}\right)\sin\left(\frac{\vartheta_R}{2}\right) \qquad (4)$$

for the spin-up ABS energies at the right interface. Spin-down states are found from $N_\sigma(x,\varepsilon)=N_{\bar{\sigma}}(x,-\varepsilon)$. The variable $\psi=\arcsin(\varepsilon/\Delta)$ contains the energy dependence. ABS positions thus not only depend on the spin-mixing angle but also on the interface distance L and the magnetization configuration. For lower ρ (higher transmissions), the DOS peaks are broadened into resonances.

In Fig. 3, the spin-up DOS at the right interface ($x=L$) is plotted as a function of the interface distance L and the spin-mixing angle ϑ. For the P configuration, one obtains a single spin-up ABS at $\varepsilon_\infty^P=\Delta\cos(\frac{\vartheta}{2})$ in the limit $L/\xi\to\infty$. This state splits in two as soon as the interface distance L is decreased. This can be interpreted as follows: the ABSs originating at both interfaces [see Fig. 2(a)] having the same energy in the limit $L/\xi\to\infty$, repel each other as the interfaces are brought closer. To first order, the energy correction to ε_∞^P is given by $\delta\varepsilon^P=\Delta\sin^2(\frac{\vartheta}{2})e^{-(L/\xi)\sin(\vartheta/2)}$, assuming $\delta\varepsilon\ll|\Delta-\varepsilon_\infty^P|$. So the repulsion strength increases with ϑ. Below a critical interface distance L_{crit}, the higher energy state is pushed out of the SC gap; close to the gap, its energy can be approximated by $\Delta-2\Delta[(L/\xi)-\cot(\frac{\vartheta}{2})]^2/[1+(L/\xi)^2]^2$. The critical distance is thus given by $L_{crit}=\xi\cot(\frac{\vartheta}{2})$. At these small lengths, the lower energy state goes like $\varepsilon_0^P+2\Delta\sin^2(\frac{\vartheta}{2})(1-e^{-(L/\xi)\sin\vartheta})$ with $\varepsilon_0^P=\Delta\cos(\vartheta)$ its energy for $L=0$. When $\vartheta>\frac{\pi}{2}$, a zero-

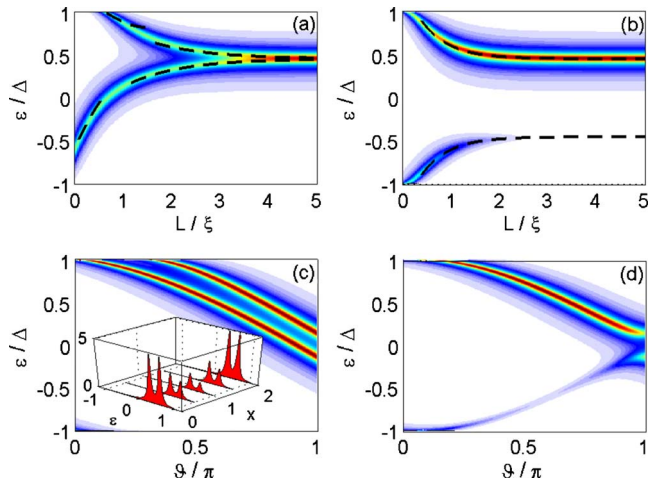

FIG. 3. (Color online) Spin-up DOS at the right interface vs L (upper panel) and ϑ (lower panel), both for [(a)–(c)] P and [(b)–(d)] AP magnetization. Dashed lines are analytical approximations (see text). Inset: propagation of the split ABS between the interfaces. Parameters in (a) and (b): $\rho=0.9$ and $\vartheta=0.7\pi$. In (c) and (d): $\rho=0.9$ and $L=2.0\xi$. Inset: $\vartheta=0.7\pi$ and $L=2.0\xi$.

bias state exists for $L=\xi \ln|\tan(\frac{\vartheta}{2})|$. The propagation of ABS split peaks through the SC is sketched in the inset of Fig. 3(c).

In the AP case, there are two ABS at energies $\pm\varepsilon_{\infty}^{\mathrm{AP}} = \pm\Delta\cos(\frac{\vartheta}{2})$ in the limit $L/\xi\to\infty$. In terms of Fig. 2(b), the negative energy state corresponds to the ABS that propagated from the other interface. Its weight is therefore reduced (it is zero for $L/\xi\to\infty$). As the interface distance decreases, this state gains weight and both ABS repel each other, entering the continuum at $L=0$. To first order, their energies are $\pm\varepsilon_{\infty}^{\mathrm{AP}} \pm \frac{1}{2}\Delta\tan\frac{\vartheta}{2}e^{-(2L/\xi)\sin(\vartheta/2)}$.

The influence of the spin-mixing angle ϑ is depicted in Figs. 3(c) and 3(d). Increasing ϑ moves all states deeper inside the gap. For the P case, the second ABS only appears for values $\vartheta>2\arctan(L/\xi)$. In the AP case, the negative-energy state is weakened as it must propagate through the SC to reach the right interface.

The ABS show up in the transport properties of FM/SC/FM heterostructures, in particular, in the NL conductance G_{NL}. Assuming a constant current density j over the contact area, the spin-resolved NL current is

$$I_{\mathrm{R}\sigma} = \frac{\mathcal{S}_{\mathrm{L}}\mathcal{S}_{\mathrm{R}}\cos(\theta_{\mathrm{L}})\cos(\theta_{\mathrm{R}})}{L^2} j_{\sigma}, \tag{5}$$

where $\mathcal{S}_{\mathrm{L(R)}}$ is the area of the left (right) contact, L again the distance between the contacts, and $\theta_{\mathrm{L(R)}}$ is the impact angle at the left (right) interface (see Fig. 1). The current density $\vec{j}_{\sigma}$ at a point $\vec{R}$ in the right electrode is $\vec{j}_{\sigma}=eN_{\sigma}\int\frac{d\varepsilon}{8\pi i}\mathrm{Tr}\langle\tau_3\vec{v}_{\mathrm{F}\sigma}\hat{g}_{\sigma}^{K}(\vec{v}_{\mathrm{F}\sigma},\vec{R},\varepsilon)\rangle$, where N_{σ} is the normal state DOS for spin σ in the right FM. G_{NL} is given by $G_{\mathrm{NL}\uparrow}+G_{\mathrm{NL}\downarrow}$ with $G_{\mathrm{NL}\sigma}=\partial I_{\mathrm{R}\sigma}/\partial V_{\mathrm{L}}$, where V_{L} is the left lead voltage. Only the trajectory connecting both contacts contributes to G_{NL} and the relevant Keldysh GF $\hat{g}_{\sigma}^{K}$ can be calculated from a generalization of Eq. (1) and the boundary conditions at the interfaces.[17]

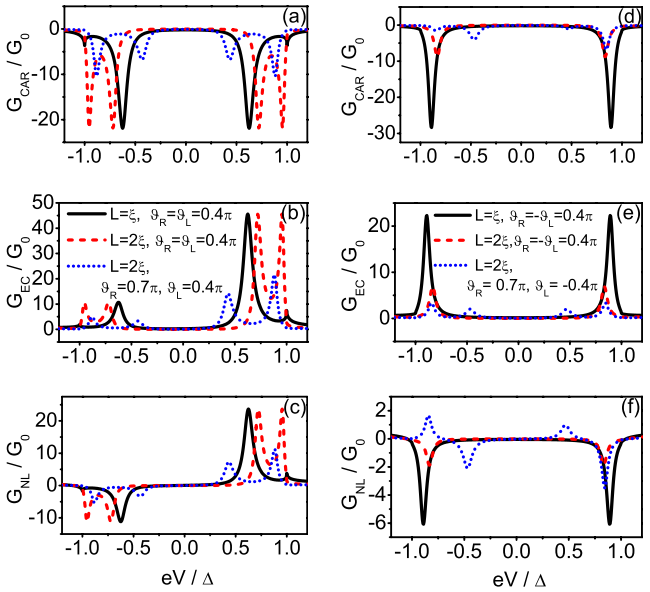

FIG. 4. (Color online) CAR and EC contributions for [(a)–(c)] P and [(d)–(f)] AP magnetization of the FM contacts. Transmission coefficients: [(a)–(c)]: $t_{\sigma}^{\mathrm{L}}=t_{\sigma}^{\mathrm{R}}$, [(d)–(f)]: $t_{\sigma}^{\mathrm{L}}=t_{\bar{\sigma}}^{\mathrm{R}}$ with $|t_{\uparrow}^{\mathrm{R}}|^2=0.14$ and $|t_{\downarrow}^{\mathrm{R}}|^2=0.07$. For other parameters see legends of (b) and (e).

The clearest ABS signature occurs for high spin-mixing angles (ABS deep inside the gap) and for the tunneling limit (ABS narrow and well defined). Figure 4 shows G_{NL} for such a set of parameters. A peaked structure is visible, hinting at the subgap states, with a marked voltage asymmetry in the case of P magnetization. These observations will now be explained with the help of Fig. 5.

For voltages eV_{L} that align the Fermi energy in the left FM with a spin-resolved ABS energy ε_{b} in the SC, a quasiparticle with the corresponding spin can tunnel from the FM into the SC. In case of EC, the particle has to tunnel to the same spin band at the same energy in the right electrode, while for CAR, an electron with energy $-\varepsilon_{\mathrm{b}}$ in the opposite spin band at the right interface is absorbed by the SC to form a Cooper pair (see Fig. 5). Both CAR and EC thus involve (to lowest order) two transmission processes. The peak height in $G_{\mathrm{NL}\sigma}$ at voltage $eV_{\mathrm{L}}=\pm\varepsilon_{\mathrm{b}}$ is given by $\mathcal{T}_{\sigma\pm}^{\mathrm{L}}\cdot\mathcal{T}_{\sigma\pm}^{\mathrm{R}}$ for EC and $\mathcal{T}_{\bar{\sigma}\pm}^{\mathrm{L}}\cdot\mathcal{T}_{\sigma\mp}^{\mathrm{R}}$ for CAR, where the $\mathcal{T}$ are effective transmission coefficients involving the product of the relevant spin-resolved transmission probability and ABS peak height at the left and right interface. The relative height of CAR and EC peaks in different magnetization geometries can be fully understood with this simple picture.

As an example, we consider $|t_{\uparrow(\downarrow)}^{\mathrm{L}}|^2=|t_{\uparrow}^{\mathrm{R}}|^2\equiv T$ and $|t_{\downarrow(\uparrow)}^{\mathrm{L}}|^2=|t_{\downarrow}^{\mathrm{R}}|^2\equiv\tau$ with $\tau<T\ll 1$ in the P (AP) configuration sketched in Fig. 5. In the P case, there is a single spin-resolved state at energies $\pm\varepsilon_{\mathrm{b}}$ and all states have the same weight W_{P} at the interfaces. The EC conductance peak thus scales as $\mathcal{T}_{\uparrow+}^{\mathrm{L}}\mathcal{T}_{\uparrow+}^{\mathrm{R}}=T^2W_{\mathrm{P}}^2$ ($\mathcal{T}_{\downarrow-}^{\mathrm{L}}\mathcal{T}_{\downarrow-}^{\mathrm{R}}=\tau^2W_{\mathrm{P}}^2$) for positive (negative) energies and the voltage asymmetry in the EC signal in Fig. 4(a) is due to the different transmissions for spin up and spin down. The CAR conductance scales as

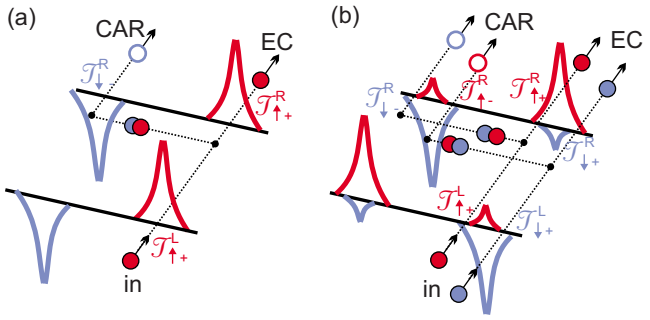

		parallel		antiparallel	
	eV_L	spin-up	spin-down	spin-up	spin-down
CAR	$+\varepsilon_b$	0	$-T\tau W_P^2$	$-T^2 w_{AP} W_{AP}$	$-\tau^2 w_{AP} W_{AP}$
	$-\varepsilon_b$	$-T\tau W_P^2$	0	$-T^2 w_{AP} W_{AP}$	$-\tau^2 w_{AP} W_{AP}$
EC	$+\varepsilon_b$	$T^2 W_P^2$	0	$T\tau w_{AP} W_{AP}$	$T\tau w_{AP} W_{AP}$
	$-\varepsilon_b$	0	$\tau^2 W_P^2$	$T\tau w_{AP} W_{AP}$	$T\tau w_{AP} W_{AP}$
$G_{NL\uparrow}+G_{NL\downarrow}$	$+\varepsilon_b$	$T(T-\tau)W_P^2$		$-(T-\tau)^2 w_{AP} W_{AP}$	
	$-\varepsilon_b$	$-\tau(T-\tau)W_P^2$		$-(T-\tau)^2 w_{AP} W_{AP}$	
$G_{NL\uparrow}-G_{NL\downarrow}$	$+\varepsilon_b$	$T(T+\tau)W_P^2$		$-(T+\tau)(T-\tau) w_{AP} W_{AP}$	
	$-\varepsilon_b$	$-\tau(T+\tau)W_P^2$		$-(T+\tau)(T-\tau) w_{AP} W_{AP}$	

FIG. 5. (Color online) Sketch of the spin-up (positive axis) and spin-down (negative axis) Andreev states at the FM/SC interfaces for (a) P and (b) AP orientation of the contact magnetizations. CAR and EC processes are shown and expressions for obtaining their relative size are given in the table.

$-\mathcal{T}^L_{\uparrow+}\mathcal{T}^R_{\downarrow-}=-\mathcal{T}^L_{\downarrow-}\mathcal{T}^R_{\uparrow+}=-T\tau W_P^2$, both for $eV_L=\pm\varepsilon_b$, and is therefore symmetric in eV_L. As a result, the total NL conductance in Fig. 4(c) changes sign so that one could switch between CAR or EC by tuning eV_L. The splitting of the conductance peaks for longer lengths [dashed curves in Figs. 4(a)–4(c)] is due to the ABS repulsion discussed in Fig. 3(a). In the AP case, both spin states are present at every ABS energy so CAR and EC contain a contribution from each one. The relevant expressions are summarized in Fig. 5. We define $w_{AP}(W_{AP})$ as the height of the smaller (larger) ABS peak (for Fig. 4, solid lines, $[wW]_{AP}=0.45W_P^2$). In agreement with Figs. 4(d)–4(f), CAR and EC are now found to be symmetric in eV_L.

In more general cases, where $|\vartheta_L|\neq|\vartheta_R|$ as in the dotted curves in Fig. 4, the total NL conductance shows peaks at four ABS energies (compare to Fig. 2). Their weight can be determined analogously to the considerations above. For example, for Fig. 2(c) and 2(d) there are bound states at $\pm\varepsilon_{b1}$ and $\pm\varepsilon_{b2}$ (with $|\varepsilon_{b1}|>|\varepsilon_{b2}|$). For the P case, similar expressions as in Fig. 5 hold with W_P^2 replaced by $[w_\ell W_\ell]_P$, where $\ell\in\{1,2\}$ labels the bound states. In the AP case, the EC contribution at $\pm\varepsilon_{b\ell}$ is $T\tau[w_\ell W_\ell]_{AP}$ and the CAR contributions are asymmetric in voltage: for $eV_L=\{-\varepsilon_{b1},-\varepsilon_{b2},\varepsilon_{b2},\varepsilon_{b1}\}$ they are $\{-\tau^2,-T^2\gamma,-\tau^2\gamma,-T^2\}[w_1W_1]_{AP}$ with $\gamma=[w_2W_2/w_1W_1]_{AP}$.[19] The corresponding relative contributions to G_{NL} are $\{\tau,-T\gamma,\tau\gamma,-T\}(T-\tau)[w_1W_1]_{AP}$.

In Fig. 5, we also discuss the spin currents $G_{NL\uparrow}-G_{NL\downarrow}$ resulting from CAR and EC processes. Interestingly, in the AP case the nonlocal spin current results solely from the CAR process as the EC contributions cancel in the tunneling limit. In contrast, for the P case, CAR and EC currents in the right lead are both fully spin polarized.

In conclusion, we studied subgap Andreev states in a FM/SC/FM setup. Due to an interaction between the bound states induced at the two SC/FM interfaces, their energetic positions depend on the relative interface magnetization orientation. This leads to asymmetries of the NL conductance, which we explain in terms of CAR and EC processes with a simple picture based on the Andreev state positions and their weight, thereby clarifying the role of Andreev states in NL conductance experiments.

[1] X.-L. Qi and S.-C. Zhang, Phys. Today **63**(1), 33 (2010).
[2] G. Deutscher, Rev. Mod. Phys. **77**, 109 (2005).
[3] M. J. DeWeert and G. B. Arnold, Phys. Rev. Lett. **55**, 1522 (1985); T. Tokuyasu, J. A. Sauls, and D. Rainer, Phys. Rev. B **38**, 8823 (1988).
[4] M. Fogelström, Phys. Rev. B **62**, 11812 (2000).
[5] A. Cottet and W. Belzig, Phys. Rev. B **77**, 064517 (2008).
[6] R. Grein, T. Löfwander, G. Metalidis, and M. Eschrig, Phys. Rev. B **81**, 094508 (2010).
[7] M. Eschrig, J. Kopu, J. C. Cuevas, and G. Schön, Phys. Rev. Lett. **90**, 137003 (2003); M. Eschrig and T. Löfwander, Nat. Phys. **4**, 138 (2008).
[8] R. Grein, M. Eschrig, G. Metalidis, and G. Schön, Phys. Rev. Lett. **102**, 227005 (2009).
[9] G. Deutscher and D. Feinberg, Appl. Phys. Lett. **76**, 487 (2000).
[10] D. Beckmann, H. B. Weber, and H. v. Lohneysen, Phys. Rev. Lett. **93**, 197003 (2004); D. Beckmann and H. v. Lohneysen, Appl. Phys. A: Mater. Sci. Process. **89**, 603 (2007); S. Russo, M. Kroug, T. M. Klapwijk, and A. F. Morpurgo, Phys. Rev. Lett. **95**, 027002 (2005); P. Cadden-Zimansky and V. Chandrasekhar, *ibid.* **97**, 237003 (2006); New J. Phys. **9**, 116 (2007); Nat. Phys. **5**, 393 (2009).
[11] G. Falci, D. Feinberg, and F. W. J. Hekking, Europhys. Lett. **54**, 255 (2001).
[12] R. Mélin and D. Feinberg, Phys. Rev. B **70**, 174509 (2004).
[13] T. Yamashita, S. Takahashi, and S. Maekawa, Phys. Rev. B **68**, 174504 (2003).
[14] M. S. Kalenkov and A. D. Zaikin, Phys. Rev. B **76**, 224506 (2007).
[15] A. L. Yeyati, F. S. Bergeret, A. Martín-Rodero, and T. M. Klapwijk, Nat. Phys. **3**, 455 (2007); D. S. Golubev and A. D. Zaikin, EPL **86**, 37009 (2009).
[16] D. Feinberg, Eur. Phys. J. B **36**, 419 (2003); R. Mélin, Phys. Rev. B **73**, 174512 (2006); A. Brinkman and A. A. Golubov, *ibid.* **74**, 214512 (2006); J. P. Morten, A. Brataas, and W. Belzig, *ibid.* **74**, 214510 (2006); D. S. Golubev and A. D. Zaikin, *ibid.* **76**, 184510 (2007); D. S. Golubev, M. S. Kalenkov, and A. D. Zaikin, Phys. Rev. Lett. **103**, 067006 (2009).
[17] M. Eschrig, Phys. Rev. B **80**, 134511 (2009).
[18] M. Eschrig, Phys. Rev. B **61**, 9061 (2000).
[19] For Fig. 4, dotted lines, [(a)–(c)]: $\gamma=0.67$ and [(d)–(f)]: $\gamma=0.61$.